Room temperature electron beam sensitive viscoplastic response of ultra-ductile amorphous olivine films

Andrey Orekhov, Nicolas Gauquelin, Guillaume Kermouche, Alejandro Gomez-Perez, Paul Baral, Ralf Dohmen, Michaël Coulombier, Johan Verbeeck, Jean Pierre Raskin, Thomas Pardoen, et al.

Full length article

Room temperature electron beam sensitive viscoplastic response of ultra-ductile amorphous olivine films

Andrey Orekhov [a,b], Nicolas Gauquelin [b], Guillaume Kermouche [c], Alejandro Gomez-Perez [d], Paul Baral [a,e], Ralf Dohmen [f], Michaël Coulombier [a], Johan Verbeeck [b], Jean Pierre Raskin [g], Thomas Pardoen [a,h], Dominique Schryvers [b], Jun Lin [i], Patrick Cordier [j,k,*], Hosni Idrissi [a,b]

[a] Institute of Mechanics, Materials and Civil Engineering (IMMC), UCLouvain, B-1348, Louvain-la-Neuve, Belgium
[b] EMAT, University of Antwerp, Groenenborgerlaan 171, B-2020, Antwerp, Belgium
[c] Mines Saint Etienne, Univ Lyon, CNRS UMR5307, LGF, Centre SMS, 158 Cours Fauriel, 42023 Saint-Etienne, France
[d] NanoMegas SPRL, Boulevard Edmond Machtens 79, B1080 Brussels, Belgium
[e] Mines Saint-Etienne, Univ Lyon, CNRS UMR 5307, LGF, Centre SMS, 158 Cours Fauriel, 42023 Saint-Etienne, France
[f] Institut für Geologie, Mineralogie und Geophysik, Ruhr-Universität Bochum, D-44801 Bochum, Germany
[g] Institute of Information and Communication Technologies, Electronics and Applied Mathematics (ICTEAM), UCLouvain, B-1348, Louvain-la-Neuve, Belgium
[h] WEL research Institute, avenue Pasteur 6, 1300 Wavre, Belgium
[i] ICSM, CEA, CNRS, ENSCM, Univ Montpellier, Marcoule, France
[j] Univ. Lille, CNRS, INRAE, Centrale Lille, UMR 8207 - UMET - Unité Matériaux et Transformations, F-59000 Lille, France
[k] Institut Universitaire de France, F-75005 Paris, France

ARTICLE INFO

ABSTRACT

The mechanical properties of amorphous olivine (a-olivine) deformed at room temperature are investigated *in situ* in a TEM under uniaxial tension using a Push-to-Pull (PTP) device. Thin films of a-olivine were produced by pulsed laser deposition (PLD). With or without electron irradiation, a-olivine films deform plastically, with a gradual transition that makes impossible the determination of a precise threshold. The strength attains values up to 2.5 GPa. The increasing strain-rate in load control results in an apparent softening with stress drop. The fracture strain reaches values close to 30 % without e-beam irradiation. Under electron illumination at 200 kV, the strength is lower, around 1.7 GPa, while higher elongations close to 36 % are obtained. Alternating beam-off and beam-on sequences lead to exceptionally large fracture strains equal to 68 % at 200 kV and 139 % at 80 kV. EELS measurements were performed to characterize the interaction between the electron beam and a-olivine. At a voltage of 80 kV, radiolysis accompanied by oxygen release dominates whereas at high voltage (300 kV) the interaction is dominated by knock-on type defects. Radiolysis is also the main interaction mechanism at 200 kV with low exposition which corresponds to most of our *in situ* TEM deformation experiments. To interpret the mechanical data, a simple 1D model has been developed to rationalize the load transfer between the PTP device and the specimen. The strain-rate sensitivity is 6 to 10 times higher when a-olivine is deformed under electron irradiation.

1. Introduction

Among silicate glasses, those with olivine composition (*i.e.* M_2SiO_4 with M=Mg, Fe, Mn,…) have been relatively little studied, largely due to the difficulty of preparing such samples by quenching from the melt [1]. The first reported observation of olivine glass was provided by Jeanloz et al. [2] from olivine specimens recovered from shock experiments at 56 GPa. The formation of this glass was then observed in static

compression experiments in a laser-heated diamond anvil cell [3]. Beyond the obvious importance of this composition in Earth sciences (olivine in its crystalline form is the main component of the Earth's upper mantle), the study of olivine glasses is of fundamental interest. Contrary to amorphous silica which is made of a polymerized network of SiO_4 tetrahedra connected through their O vertices, amorphous olivine is dominated by isolated, non-polymerized SiO_4 tetrahedra, separated by M^{2+} polyhedra. More specifically, interest in this compound was

revived when grain boundary amorphization was reported in olivine aggregate deformation experiments [4]. Stress-induced amorphization of grain boundaries appears as a potential deformation mechanism under high stress [5], and in the particular case of olivine, this mechanism has been proposed as possibly being the cause of the drop in viscosity at the boundary between the lithosphere and the asthenosphere as the glass passes the glass transition temperature [6]. It therefore appears necessary to study the mechanical properties of olivine glasses. While glasses are usually brittle materials, it has been shown that ductility can be enhanced at small scales [7,8]. This is particularly relevant in the case of amorphized grain boundaries, which can be nanometric in thickness.

In this study, we investigate the mechanical properties of amorphous olivine using micromechanical tensile tests in a transmission electron microscope (TEM). Recent works have shown that electron irradiation has a significant influence on the mechanical properties of amorphous silica [9], so particular attention is paid to this phenomenon.

2. Material and methods

2.1. Pulsed laser deposition (PLD) of amorphous olivine (a-olivine) films

For the preparation of thin films, polycrystalline pellets of synthetic olivine with a nominal composition of $Fe_{0.2}Mg_{1.8}SiO_4$ were ablated using a pulsed laser beam with a frequency of 10 Hz, a wavelength of 193 nm, and at a laser fluence of approximately 5 J/cm^2. Details on the setup can be found in Dohmen et al. [10]. The deposition rates were in the range 10–20 nm/min. The depositions were performed at a background vacuum pressure of 1×10^{-3} Pa and at room temperature. Under these conditions, it has been demonstrated [10] that the silicate film of an olivine-like composition is amorphous and chemically homogeneous. The depositions were performed on clean [100] oriented silicon wafers. The resulting surface topography is small with a typical roughness of <1 nm [10], as measured by atomic force microscopy (AFM). The PLD set-up does not allow the rotation of the substrate during deposition and the plasma jet coming out of the target is relatively small compared to the substrate. This results in a deposited layer with some variation of the thickness (see Fig. 6c in [10]). The thickness has to be measured for every sample used for quantitative nanomechanical tensile testing *in situ* in the TEM for accurate estimation of the applied stress.

2.2. TEM characterizations

The initial microstructure was investigated on classical Focused Ion Beam (FIB) cross-sections of a-olivine deposited on a Si substrate. A Pt protection layer was deposited in two steps – by electron beam, then by ion beam– in order to minimize FIB damage at the sample surface. The FIB foils were thinned to a thickness < 50 nm. An ion beam of 2 kV/0.2 nA was employed for final thinning of the specimen and to minimize irradiation damage generated during high-voltage FIB thinning. TEM characterizations were conducted in a FEI Osiris microscope equipped with highly efficient SuperX Energy Dispersive X-ray (EDX) system operated at 200 kV. Z-contrast images were recorded in scanning transmission electron microscope (STEM) mode with convergence angles of 115–157 mrad using an HAADF-STEM detector. Selected area electron diffraction (SAED) patterns were used to calculate the "Reduced Pair Distribution Function" G(r) [11]. The *e-PDFSuite* software [12] was used for data reduction following a procedure detailed in Juhas et al. [12]. First the data is azimuthally integrated in an equidistant Q-grid obtaining a 1D I(Q) graph that will be used for the final calculation. Since the sample was prepared as a FIB lamella, no further corrections-subtractions have to be performed because the interaction of the beam is only with the sample and not with any other container or support grid. The calculation of the structure function S(Q) and the derived one F(Q) are made exactly as described in [12] with the only difference of using the electron form factors instead of x-ray form factors. The r-poly function was used for background corrections of the F

(Q), basically consisting on a n-degree polynomic fitting that has to take into account the shortest physical bond-distance in the sample and the $Q_{MAXINST}$ obtained during measurements. Then G(r) was calculated by normalization and Fourier transformation [13–15]. The parameters applied for the Fourier transformation were: integral limits $Q_{MAX} = 15$ Å^{-1} and $Q_{MIN} = 0.82$ Å^{-1}; R-grid plot in real space with 0.05 Å step from 0 to 10 Å.

Electron energy loss spectroscopy (EELS) was used to investigate the effect of e-beam irradiation on the a-olivine films. EELS measurements at 80 kV and 300 kV were performed on a Titan 80–300 double aberration corrected microscope equipped with a monochromator and a Gatan K2 direct electron detection camera (3710 pixels) mounted on a Gatan Quantum spectrometer. At 300 kV, the energy resolution was 0.5 eV at a dispersion of 0.25 eV/pixel used to record the O K, Fe L and Mg K edges simultaneously and 0.2 eV at a dispersion of 0.025 eV/pixel used to record the Si L edge. At 80 kV, the energy resolution was 0.3 eV at a dispersion of 0.15 eV/pixel used to record the O K and Fe L edges simultaneously and 0.17 eV at a dispersion of 0.025 eV/pixel to record the Si L edge. EELS measurements at 200 kV were performed on a Titan 60–300 probe aberration corrected microscope equipped with a monochromator and a Gatan Enfinium spectrometer (2048 pixels), the energy resolution was 1 eV at a dispersion of 0.25 eV/pixel used to record the O K and Fe L edges simultaneously and 0.2 eV at a dispersion of 0.025 eV/pixel to record the Si L edge. At each voltage, the dose was varied by changing the spot size from 14 to 17, as can be seen in Table 1, resulting in a slight defocus of the electron probe. The electron doses corresponding to those conditions are reported in Table 2. 600 spectra were acquired with an acquisition time of 0.2 s/spectra. For each measurement, a new fresh area of the sample was used. To maximize the visibility of the damage, the probe was kept at a constant position and spectra recorded as a function of time.

2.3. In situ TEM nanomechanical testing

Freestanding a-olivine thin films have been produced in the context of another study [16] designed to perform nanomechanical tensile testing as shown in Fig. 1a. In the present work, undeformed freestanding beams were cut (Fig. 1b) using a dual-beam FIB/SEM instrument (FEI Helios Nanolab 650) equipped with an Omniprobe micromanipulator (Oxford Instruments plc, Tubney Woods, UK). Pt deposition was then used to attach the beam on a push-to-pull (PTP) device (PI 95 TEM PicoIndenter instrument from Bruker, see Fig. 1c) for *in situ* TEM tensile experiments [17,18]. A dog bone shape was thus obtained by FIB (Fig. 1d). This approach allows avoiding FIB thinning that might alter the initial glassy microstructure and the resulting mechanical properties.

Quantitative tensile experiments with PTP were performed under load control mode. The applied force on the specimen was determined by removing the contribution of the PTP spring stiffness from the raw force. PTP stiffness was measured by performing a load-unload cycle after the tensile experiment (when the sample is broken). The engineering stress was calculated by dividing the force by the initial cross-sectional area of the specimen. The sample thickness was measured in high-resolution mode of SEM with a resolution better than 10 nm. Videos with rate of 5 frames/*sec* were recorded and post-processed using

Table 1
Maximum probe diameters (in Angstroms) corresponding to EELS measurements. SS14 corresponds to spot size 14, SS17 corresponds to spot size 17.

Voltage	SS14		SS17	
	Probe diameter (Å)	Beam current (pA)	Probe diameter (Å)	Beam current (pA)
80 kV	8	260	2.8	40
200 kV	6.5	360	2	50
300 kV	4	440	1.5	80

Table 2

Electron dose corresponding to the EELS measurements. SS14 corresponds to spot size 14, SS17 corresponds to spot size 17.

Voltage	SS14 Electron dose rate (e^-/nm^2/s)	SS17 Electron dose rate (e^-/nm^2/s)
80 kV	8.16 10^8	1.54 10^7
200 kV	7.46 10^8	9.80 10^6
300 kV	3.45 10^8	8.82 10^6

home-made MATLAB scripts. The engineering strain was extracted by measuring the displacement directly in the gauge section of the specimen using digital image correlation (DIC). The effect of the electron beam on the mechanical response of the films was investigated by performing beam-off and beam-on PTP experiments with controlled electron doses at 200 kV and at 80 kV.

3. Results

3.1. PLD amorphous olivine characterization

PLD a-olivine films have already been the subject of chemical and microstructural characterizations [10,16]. The selected area diffraction pattern (SAED) given in Fig. 2 shows the presence of two diffuse rings which confirms the amorphous structure. In this figure, a pair distribution function (PDF) G(r) calculated from the same SAED pattern

shows two main peaks located at 1.6 and 2 Å which correspond to the Si-O and Mg-O medium range order (MRO), respectively [19].

3.2. In situ TEM nanomechanical testing

Table 3 summarizes the characteristics of the PTP specimens used in the present work. It includes the loading rate, the PTP stiffness, the specimen dimensions, the maximum engineering strain and stress, the plastic strain at fracture, elastic modulus, the irradiation conditions (beam-on, beam-off or alternating beam-on/beam-off) as well as the voltage and electron dose. The Poisson ratio is equal to 0.5.

Fig. 3a presents in blue the variation of the engineering stress $\sigma^{eng} = \frac{F}{A_0}$ (F is the applied force, A_0 is the cross section area prior to deformation) as a function of the engineering strain $\varepsilon^{eng} = \frac{\Delta L}{L_0}$ (L_0 being the gauge length of the dog bone specimen, see Fig. 3b) corresponding to OL-1 deformed at room temperature under load control mode (loading rate 0.05 μN.s^{-1}) and beam-on condition. At this stage, the only correction is related to the PTP stiffness. It is difficult to precisely determine the yield point since the response bends progressively until a maximum engineering stress of 1.69 GPa is reached at *ca.* 12.9 % engineering strain. This is followed by an apparent softening regime which continues until rupture at 35.7 % engineering strain and 1.1 GPa engineering stress. An apparent Young's modulus, named simply "elastic modulus", was determined, see Table 3, during loading using the slope from zero strain to the point at which a deviation from the initial linear regime is
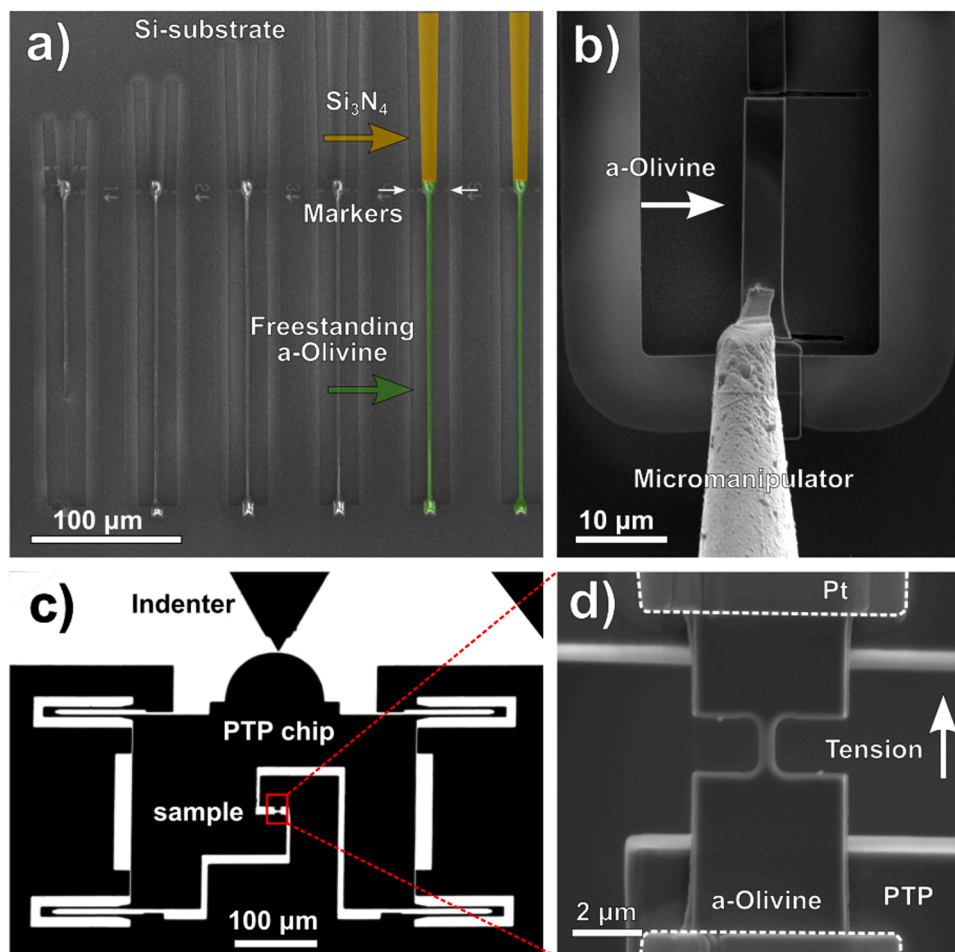
Fig. 1. a) SEM image of a freestanding amorphous olivine film (highlighted with green) and Si$_3$N$_4$ actuator (highlighted with yellow) on a lab-on-chip system before release (*i.e.* tensile deformation); see the cursors indicated by the white markers in (a); Coulombier et al. (2024) b) Magnified SEM image showing the transfer of a-olivine freestanding film on a PTP chip by a micromanipulator. c) TEM overview image of PTP chip with a-olivine sample located in center as shown in the magnified SEM image in (d).

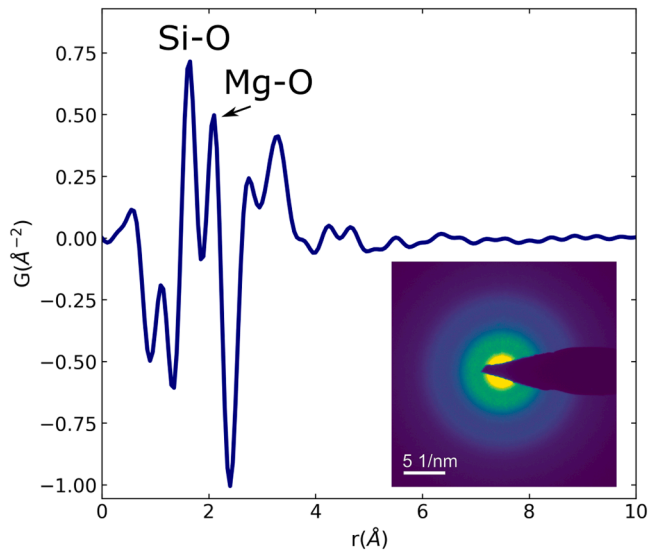**Fig. 2.** Structure of the amorphous olivine film deposited by pulsed laser deposition (PLD). Pair distribution function (PDF), G(r), calculated from the selected area electron diffraction (SAED) pattern in insert.

detected. This gives a value of 69.2 GPa for the curve of Fig. 3a. The maximum plastic strain, also reported in Table 3, is obtained by subtracting from the total strain the elastic strain which is equal to the stress at fracture divided by the elastic modulus, giving here 34 %. This very high ductility requires further stress and strain corrections to account for dimensional variations of the specimen during deformation. As the deformation is followed *in situ* in the microscope, the variation of the width can be measured during deformation, and, by simply assuming that the deformation is isotropic in each transverse section, the following correction is made (represented by the orange curve in Fig. 3a):

$$\sigma^{true\ 2} = \frac{\sigma^{eng}}{(1+\varepsilon^T)^2}; \varepsilon^{true\ 2} = \ln(1+\varepsilon^{eng}) \tag{1}$$

where ε^T is the transverse strain. Fig. 3a indicates that the stress is affected by this correction leading to a higher value of the maximum stress (close to 2 GPa) while the true fracture strain is equal to 28.8 % which still demonstrates a high ductility when expressed with a logarithm norm. Fig. 3b, 3c and 3d show snapshots before deformation, just before and after fracture, respectively. Plasticity is very stable. Necking does not start after the maximum stress is reached. Also, there is no sign of catastrophic shear banding. Hence, the fracture strain is large. Only a very slight necking is observed just before fracture as can be seen in Fig. 3c (see Fig. S1 in the Supplementary Materials for more details on necking determination). Interestingly, the intensity profiles shown in Fig. 3e show that this late necking correlates with the formation of a nanovoid at the center of the gauge section indicating that the fracture is ultimately controlled by cavitation. This void can also be observed in the zoom of Fig. 3c. These observations raise the question of the origin of the apparent softening regime emerging from Fig. 3a (*i.e.* a decrease of the true stress value).

Fig. 4a shows engineering stress-strain curves for OL-2 and OL-3 deformed without being exposed to the e-beam (beam-off) together with OL-1 with beam-on for comparison. All these experiments were performed under load-control mode with a loading rate of 0.05 µN/s. In this figure, a clear increase of strength at the expense of ductility can be observed when the e-beam is switched off. Indeed, the maximum stress (resp. fracture strain) increases (resp. decreases) from 1.7 GPa (resp. 35.7 %) under beam-on to 2.4–2.6 GPa (resp. 28.9–17.3 %) under beam-off. The apparent modulus measured under beam-off was equal to 48.1 and 38.1 GPa for OL-2 and OL-3, respectively (69.2 GPa under beam-

Table 3
Summarized technical data for all the PTP tensile experiments described in this study.

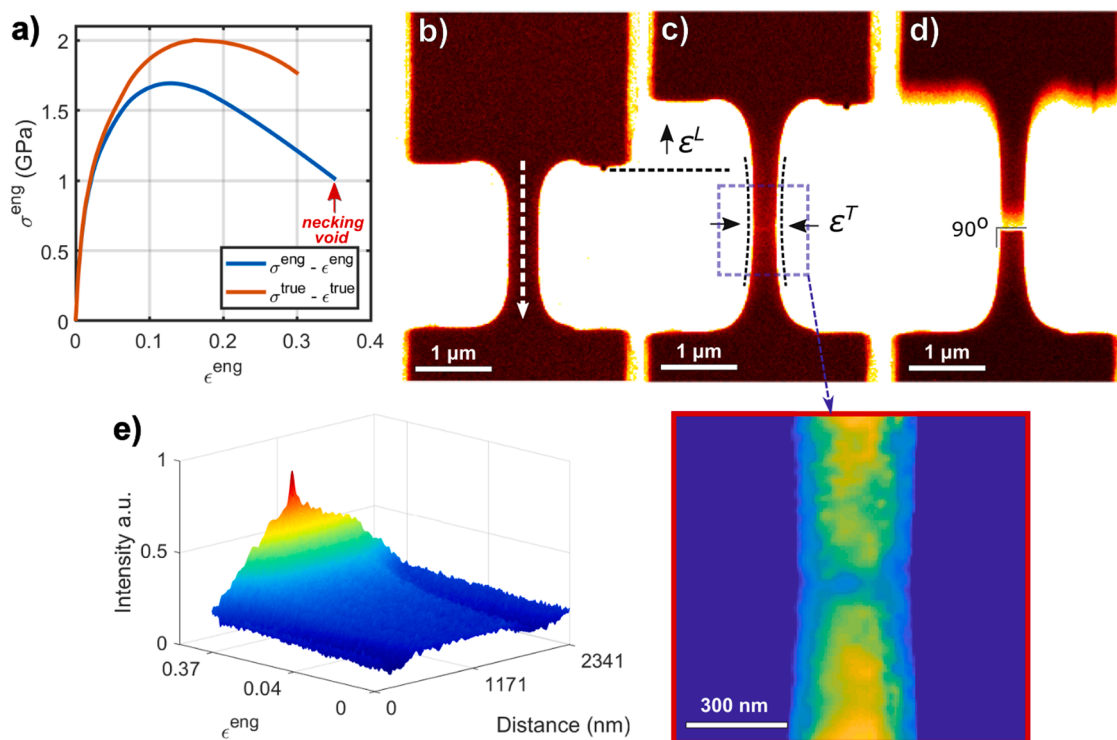| Label	Beam Mode	Load rate (µN/s)	PTP stiffness (N/m)	Sample dimensions (nm) Length / width / thickness	Max eng strain (%)	Max eng stress (GPa)	Max plastic strain (%)	Elastic modulus (GPa)	HT (kV)	Beam current (nA)	Electron dose rate (e A^{-2}s^{-1})
OL-1	On	0.05	269	2156 / 408 / 260	35.7	1.69	34	69.2	200	0.173	0.01
OL-2	Off	0.05	261	2094 / 395 / 260	28.9	2.39	24	48.1	200	–	–
OL-3	Off	0.05	286	1700 / 456 / 260	17.3	2.59	11	38.1	200	–	–
OL-4	Off, Cycles	0.1	469	1470 / 405 / 260	13.1	2.65	6.8	40.1 C1 41.9 C2 41.2 C3 40.3 C4	200	–	–
OL-5	On / Off	0.1	449	1500 / 460 / 270	68.1	1.51	64.4	37.8	200	2.47	0.11
OL-6	On / Off	0.05	204	1170 / 415 / 270	139	0.83	137.6	33.8	80	2.26	0.38

Fig. 3. a) Stress-strain curves (OL-1) calculated for engineering strain measurements (blue curve) and true stress-strain curve calculated when transverse strain is measured (orange curve). The red arrow indicates the simultaneous occurrence of necking and cavitation. b-d) Video snapshots before deformation, just before and after fracture. e) Intensity profile measured along dashed line in (b) shows the formation of a nanovoid at the center of the gage as function of the engineering strain.
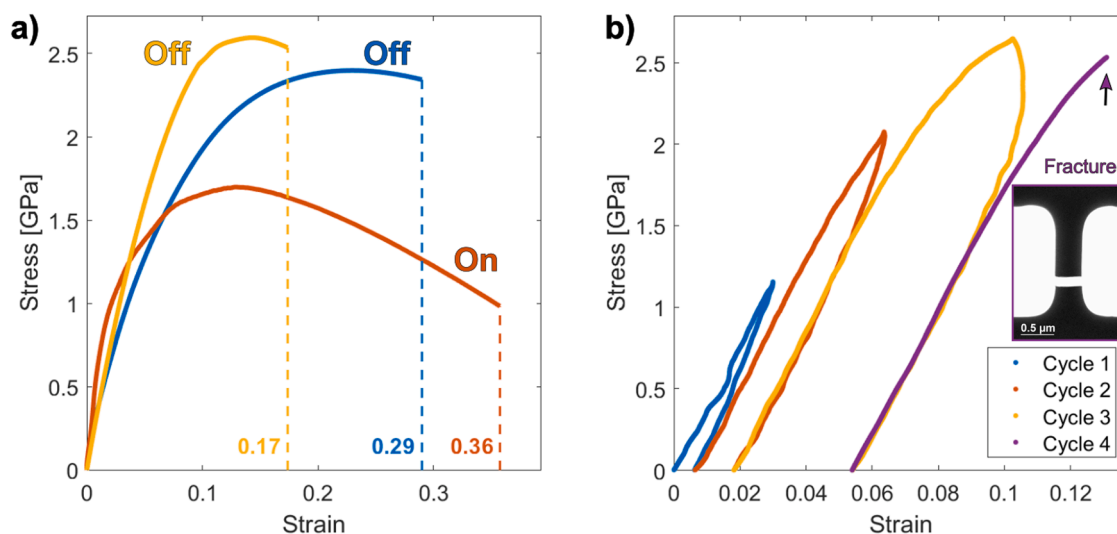

Fig. 4. a) Engineering stress-strain curves of 'beam on' (OL-1 orange) and 'beam off' (OL-2 blue and OL-3 yellow) experiments. b) Engineering stress-strain cycles of the 'beam off' (OL-4) sample.

on). The corresponding plastic strains at fracture are given in Table 3. Fig. 4b represents four deformation cycles imposed on OL-4 under load control mode with a loading rate of 0.1 μN/s and under beam-off, in terms of engineering stress-strain response for each cycle. After each cycle, the experiment was stopped in order to set the parameters of the following cycle. The maximum load was increased after each cycle. An apparent Young's modulus of 40.1 GPa (Table 3) was extracted for the first cycle. No significant variation of the modulus between cycles was observed. Note that a significant forward creep contribution occurs upon unloading leading to a hysteresis in the response. This creep deformation is related to the viscoplastic behaviour of amorphous olivine, as further

analyzed in the sequel. Fracture occurred during the fourth cycle at an applied stress of 2.53 GPa and a total accumulated strain of 13.1 %. Fig. 4b shows that plastic deformation accumulates during the cycles as evidenced by the deviation from the pure elastic regime detected at an applied stress of ~1.15 GPa for cycle 1, 2.07 GPa for cycles 2, 2.64 GPa for cycle 3, and 2.53 GPa for cycle 4. The fracture strain (expressed as total strain or plastic strain) varies from one specimen to another. This is not unexpected as the fracture strain heavily depends on the presence of defects.

Fig. 5a and 5b show force-vs-time and displacement-vs-time curves from tensile experiment for OL-5 sample under alternating beam-on and
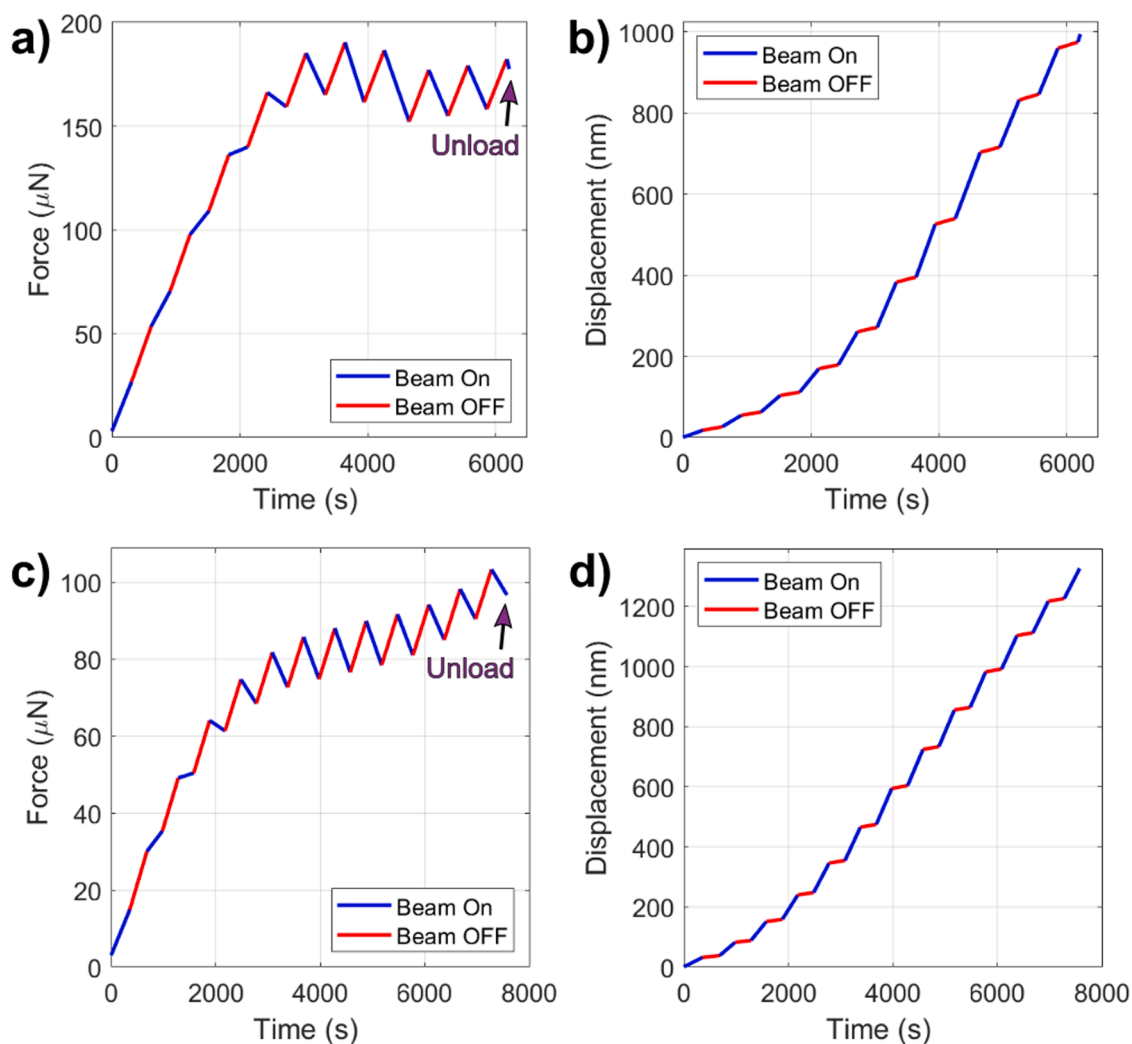
Fig. 5. PTP experiments performed at 200 kV and 80 kV with alternating beam On/Off every 5 min. (a,b) Dependence of the force and displacement applied on the sample as a function of time at 200 kV (sample OL-5). (c,d) Dependence of the force and displacement applied on the sample as a function of time at 80 kV (sample OL-6).

beam-off conditions (every 5 min) at 200 kV conducted in the load control mode. Fig. 5c and 5d show data from a similar experiment performed at 80 kV on the OL-6 sample. The results show a clear decrease (resp. increase) of the force (resp. displacement) under beam-on (resp. beam-off) condition indicating the activation of viscoplasticity mechanisms under e-beam irradiation at 80 and 200 kV.

3.3. EELS measurements under e-beam irradiation

An undeformed specimen of a-olivine was measured by EELS to probe the electron beam influence on its structure and properties (see Fig. 6 and Figs. S2, S3 and S4 in the Supplementary Materials). The study parameters are dose and voltage. EELS data acquired at 200 keV are presented in Fig. 6 together with a comparison of the O K edge fine structure at 80, 200 and 300 kV (Fig. 6e). Beam damage by electron beam can involve two mechanisms: (i) knock-on damage due to high-angle elastic electron-nucleus scattering which primarily concerns conductive materials and is all the more effective the higher the voltage; (ii) ionization damage called radiolysis due to low-angle inelastic electron-electron scattering which results in the breakup of covalent bonds, in the formation of electron-hole pairs in (semi)conductors or of radicals in organic materials and the creation of secondary electrons which may initiate further chemical reactions and further damage process. Radiolysis generally predominates at low acceleration voltage,

when the incident beam energy is just above the ionization energy [20, 21].

At 80 kV, damage by radiolysis is the main mechanism as evidenced by the presence of a strong prepeak of the O K edge, at 530 eV, which corresponds to the immediate production and the liberation from the surface of molecular O_2 [22-25] (see Figs. S2a-b). This happens regardless of the electron dose and ceases after some time of irradiation [23]. The Mg K edge was detected but disappears after less than a minute (see Fig. S3). This observation correlates with the disappearance during the first seconds of the measurement of a significant shoulder of the O K edge, which is attributed to the O-Mg bonds of forsterite character (Fig. 6e first panel). Another feature is the appearance of a shoulder at low energy (from 98 to 104 eV) on the Si L edge at high dose rate which might be a sign of some silicon with lower bonding covalency (Supplementary Fig. 2d). On the other hand, we can notice a progressive decrease of the Fe and the Si signals indicating a sputtering of heavy atomic species due to knock-on damage (see Fig. S2). In summary, in this compound, beam damage at 80 kV is mainly due to ionization, which predominantly affects Mg-O bonds and results in the departure of oxygen from the surface but not from the bulk. Some ablation of Mg from the bulk is also noted which must probably be attributed to knock-on. Ablation of Fe and Si by knock-on is also observed, but to a much lower extend.

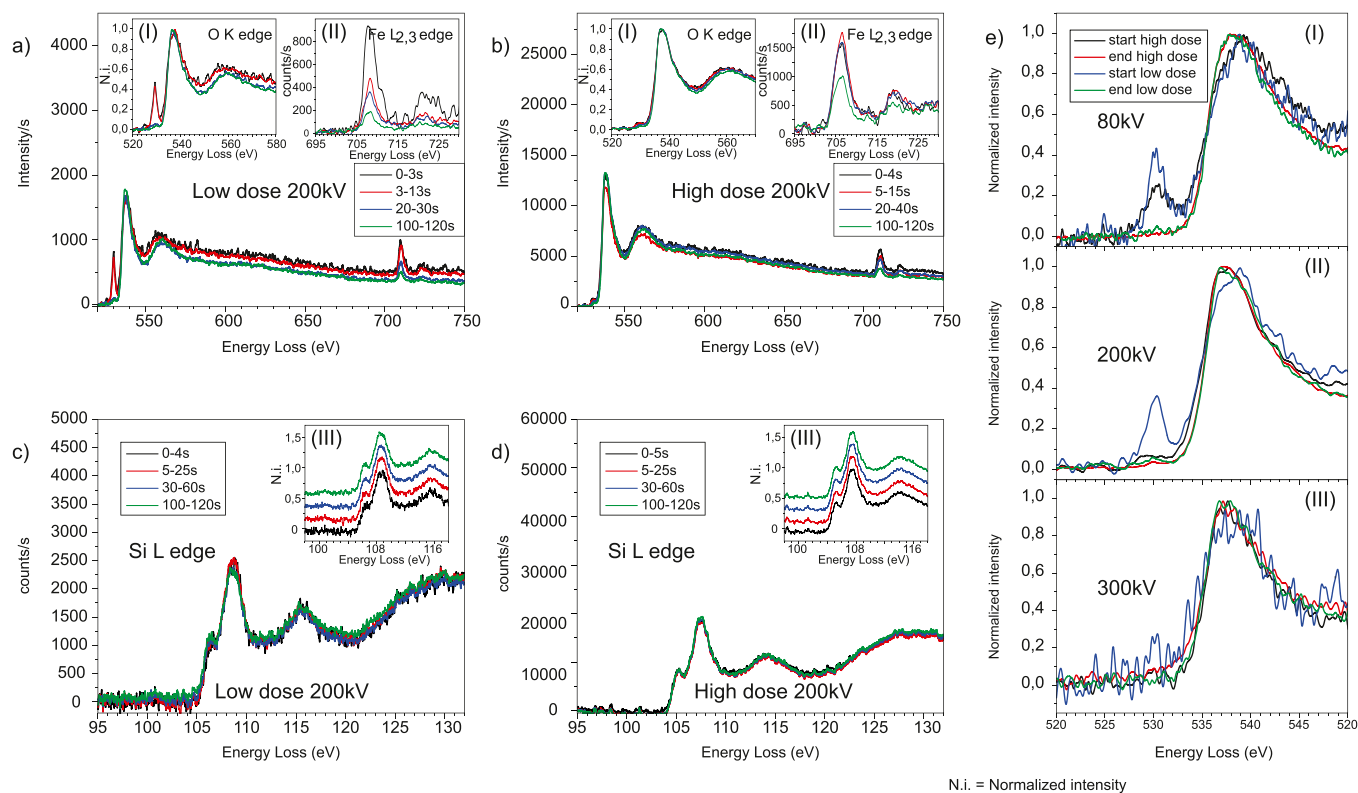At 300 kV, damage by knock-on is the dominant mechanism, as

Fig. 6. a-b) EELS spectra recorded at low dose (SS17) and high dose (SS14) respectively at 200 kV acceleration voltage. In each panel, the main graph represents the O K edge together with the Fe L edge in intensity per second, for 4 different periods during the measurement. The left inset (I) represents the O K edge fine structure evolution (the intensity has been normalized for easier comparison). The second inset (II) represents the Fe L edge in counts/second to identify the depletion in Fe. c-d) Silicon L edge EELS spectra recorded at low dose (SS17) and high dose (SS14) respectively. In each panel, the main graph represents the Si L edge in intensity per second, for 4 different periods during the measurement. The inset (III) represents the Si L edge fine structure evolution (the intensity has been normalized for easier comparison). e) Direct comparison of the O K edge ELNES recorded at low dose and high dose at the 3 different acceleration voltages (80, 200 and 300 kV from top to bottom) on amorphous olivine. For each experiment, a spectrum taken at the start of the experiment and at the end of the experiment were extracted.

evidenced by the reduction of the signals of the different elements due to sputtering seen on Fig. S4. Mg is not detected so we suppose that it is the first element to be affected. No change of fine structure is observed, the order of ablation of the elements is as follows Mg>O>Fe>Si.

The least amount of damage is observed at 200 kV since the contribution of radiolysis reduces (see Fig. 6b). Indeed, we see no change of the fine structure of the O K edge throughout the measurement (left inset in Fig. 6b (I)). Departure of oxygen results predominantly from knock-on (Fig. 6e (II)). We can notice that beam showering (broad illumination of the specimen with an intense beam) at 80 kV removes the production of molecular oxygen (prepeak to the O K edge) but the fine structure of the O K edge is then similar to the spectrum at the end of the damage measurement (no more high energy shoulder). The Mg K edge could not be measured, but observation of the shoulder of the O K edge at low dose suggest ablation of Mg by knock-on. Si and Fe are ablated by knock-on, but much less than at 300 kV. The Si L edge does not seem to change throughout the measurement, (seen on Fig. 6c-d) showing that SiO$_4$ tetrahedra are little affected. In summary, at 200 kV, electron beam damage involves both mechanisms with a stronger contribution of radiolysis at low dose and a stronger contribution of knock-on at high dose. In both cases, O and Mg are predominantly affected.

4. Discussion

When the temperature is significantly lower than the glass transition temperature T_g, silicate glasses, like silica glass, are brittle solids. Only above T_g can they be shaped, as man has learned to do since the Bronze Age [26]. It is reasonable to assume that the same applies to a-olivine, although this glass is not available in bulk form. However, it has recently

been shown on amorphous silica, whether on nanowires [27] or nanofibers [28], that significant ductility can be achieved at room temperature (*i.e.* far from T_g) at small scales. This is not a unique property of silica, since amorphous alumina, for example, exhibits the same behavior [8]. We show here that the same is true for a-olivine, which can be strained up to almost 30 % at room temperature while its T_g is of the order of 1000 K [1,29]. Plastic flow occurs at a stress of the order of 2.5 GPa. The cycles of the OL-4 experiment clearly show that the strain produced in the non-linear regime accumulates over the cycles and is indeed non-recoverable, plastic. These tests also show that creep deformation keeps accumulating during unloading, which will be discussed later. The observed apparent softening, is due to the response of the device (load controlled) to the evolution of the strain-rate (see Fig. S5 in the Supplementary Materials) and strongly depends on the strain-rate sensitivity of the specimen.

The mechanical properties of a-olivine have already been investigated at room temperature by using nanoindentation [30]. In this earlier work, the Young's modulus of a-olivine, was determined to be between 89 and 92 GPa. The values obtained under uniaxial tension with the PTP testing frame in the present work (see Table 3) are lower than those obtained by nanoindentation [30]. Indeed, the elastic modulus extracted from the PTP experiments varies between 35 and 69 GPa. Aside from uncertainty on the exact thickness, the main source of error probably comes from sample misalignment. A small deviation from perfect alignment of the specimen axis with respect to the PTP pulling direction leads to significant impact on the apparent specimen stiffness. The fact that the length of the undeformed specimen is relatively short amplifies this effect. One must also add unperfect flatness of the specimen which contribute a lot at small to moderate strain levels as the specimen gets

progressively stretched. This is why, again, other methods such as nanoindentation are more appropriate to get accurate Young's moduli. The differences could also result from the activation of relaxation mechanisms at the very early stage of deformation in the PTP tensile experiments. Uncovering the origin of such behavior requires further investigations which go beyond the scope of the present study.

The striking feature of our experiments is the marked sensitivity of a-olivine's mechanical properties to electron irradiation (Figs. 4 and 5). This phenomenon has already been revealed in amorphous silica, and has been the subject of several SEM and TEM studies [9,31-33]. Under electron irradiation (at 200 kV), there is a significant drop (of around 0.7–1 GPa) in flow stress and a significant increase in ductility (Fig. 4). The latter can even reach spectacular levels when alternating beam on/beam off episodes are applied, as one test (at 80 kV) was conducted up to 140 % elongation (without failure being reached). Fig. 5 highlights the strain-rate dependent plastic flow of a-olivine both under beam-off and beam-on conditions at both 80 and 200 kV with the same behavior being observed. Figs. 5, b and d show that a-olivine switches almost instantaneously (at the timescale of observation) between stiff and more ductile behavior, which is reflected in a change in slope of the displacement curve as a function of time. On the force *vs.* time curves (Fig. 5a,c), this translates into a drop in stress as ductility increases. A similar enhancement of the viscoplastic flow activity due to the electron beam has been reported very recently on metal thin films using a specific MEMS device allowing for displacement-controlled experiment [34]. In this study, the stress relaxation occurring when the electron beam is turned on is consistent with a rate-controlling mechanism. It is more surprising here since the constant loading rate experiment should not induce stress relaxation but rather a larger creep contribution.

Such in-between stress relaxation and creep behavior is a direct consequence of the PTP setup. In order to interpret this phenomenon, and to extract the viscoplastic response of a-olivine, we propose a simple 1D model aiming at simulating the mechanical response of olivine while taking into account the load transfer between the PTP and the sample. This model is described in the Supplementary Materials. The results are presented in Fig. 7 in terms of stress-strain curves and strain-time curves for experiments conducted at for 200 kV and 80 kV. The resulting

Table 4

PTP stiffness, Consistency parameter K and strain rate sensitivity m for alternating beam-off/beam-on for acceleration voltage 80 kV and 200 kV.

Acceleration voltage U	PTP stiffness (fitted) (N/m)	Consistency K (GPa.s^{-m})	Strain rate sensitivity m
80 kV (Ol-6)	235	71	0.55
200 kV (Ol-5)	500	26	0.34

rheological parameters and PTP stiffness are summarized in Table 4. A fairly good agreement is found between the experimental data and the results of the 1D model. It confirms the hypothesis made for the mechanical behavior of a-olivine, *i.e.* elastic-viscoplastic without any time-independent yield threshold. Both stress-relaxation and creep are very well reproduced. The peak stress is 50 % higher in the case of the 200 kV acceleration voltage. On the contrary, strain rate and strain rate sensitivity are larger under 80 kV acceleration voltage. The strain rate sensitivity is equal to 0.34 under irradiation at 200 kV, and equal to 0.55 under irradiation at 80 kV (Table 4). These very large values, typical of superplastic materials, can be compared with the strain-rate sensitivity $m = 0.05$ determined by nanoindentation [30] and from recent on-chip relaxation tests at very low strain rates down to 10^{-12} s^{-1} [16]. The strain-rate sensitivity is 6 to 10 times higher when a-olivine is deformed under e-beam irradiation.

The mechanism by which electron irradiation promotes the ductility of a-olivine may be open to question at 200 kV since our EELS measurements show that at this acceleration voltage two damage mechanisms, radiolysis and knock-on, operate. However, the fact that this effect is even more pronounced at 80 kV, where only radiolysis is active, leads us to conclude that the radiolysis mechanism is the cause of the enhanced ductility in a-olivine. This process, which is specific to dielectrics, results from inelastic interaction between incoming electrons and atomic electrons. This induces local electron excitations or complete ionization which alters bonding between atoms, so that existing bonds could break leading to the formation of other bonds [35]. Radiolysis has mainly been studied in crystalline or amorphous silica where it leads to the formation of defects associated with broken bonds between silicon and oxygen atoms: silicon dangling bonds, oxygen deficiency centers,
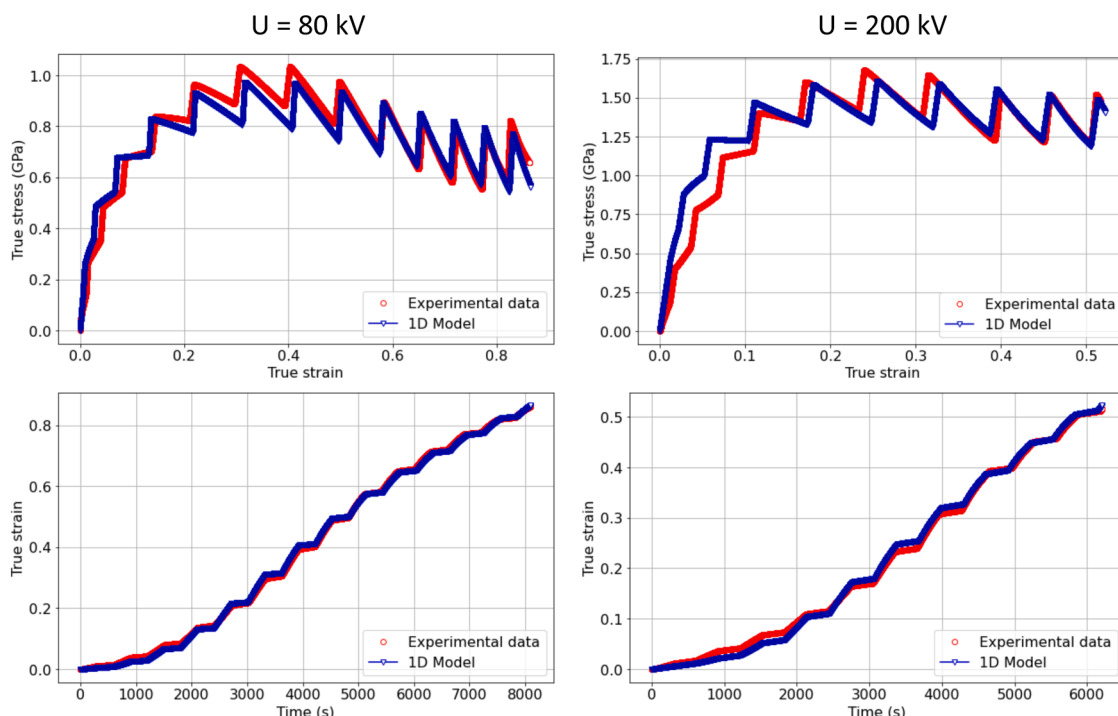

Fig. 7. comparison of experimental and numerical results of alternating beam-off/beam-on. Acceleration voltage (left: 80 kV (Ol-6) and right: 200 kV (Ol-5)).
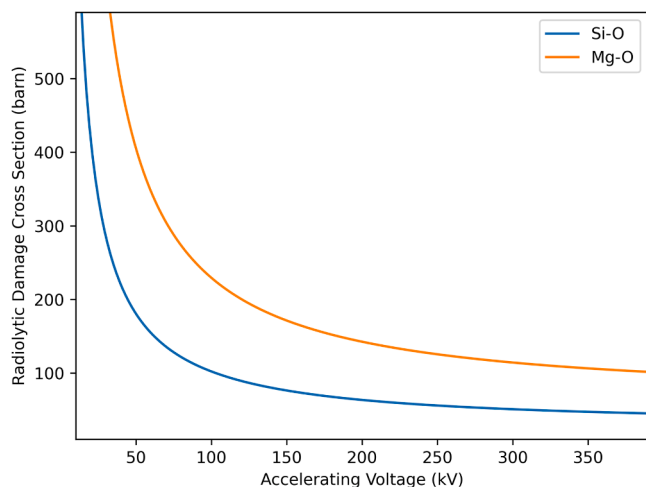
Fig. 8. Radiolytic cross section for Mg-O and Si-O bonds *versus* the kinetic energy of electrons.

non-bridging oxygen hole centers [36,37] and to the release of some oxygen molecules. This last defect is the one that gives the most discriminating signature in our EELS measurements (Fig. 6e). We find however that Si remains fourfold coordinated (Fig. 6c, d and Fig. S3c, d in the Supplementary Materials). On the other hand, it is mainly the Mg atoms (and therefore the Mg-O bonds) that are affected. To further investigate this point, we made a theoretical estimation of cross sections related to radiolytic processes. The radiolytic damage cross section, denoted by σ_r, can be expressed as $\sigma_r = \zeta \sigma_e$, as depicted in prior studies [35,38-40]. Here, ζ stands as the radiolytic efficiency factor, approximately equal to 10^{-4} as reported in literature [35], while σ_e encapsulates the cross section of a relativistic electron interacting with a specimen electron:

$$\sigma_e = \frac{8\pi a_0^2 R_\infty^2}{mc^2} \frac{Z}{T_{th}\beta^2}$$

In this expression, T_{th} denotes the dissociation energies ($\sim$8.3 eV for the Si-O bond, $\sim$3.7 eV for the Mg-O bond [41]); Z represents the number of electrons surrounding the target; a_0 symbolizes the Bohr radius; mc^2 signifies the rest mass of an electron; and R_∞ is the Rydberg constant. Additionally, β is defined as:

$$\beta = \sqrt{1 - \frac{1}{(U_b/mc^2 + 1)^2}}$$

with U_b being the incident beam energy.

Fig. 8 shows that whatever the accelerating voltage, the radiolytic damage cross section is larger for the Mg-O bonds. This demonstrates a larger sensitivity of those bonds to radiolytic damage. Fig. 8 shows also, as observed in our EELS measurements, a strongly increasing efficiency of this damage mechanism as the acceleration voltage of electrons is reduced. We therefore conclude that the electron beam assisted viscoplastic response of amorphous olivine is mostly enhanced by the perturbation of the Mg-O bonds which facilitate the activation of plastic events (in line with the shear transformation zones formalism, STZ, originally proposed by Argon [42] and then named by Falk and Langer [43]). Because of the way viscoplasticity is promoted, the role of electron irradiation can be compared with that of temperature. While these two mechanisms may be equivalent in terms of behavior, they differ in their microscopic mechanisms. Thermal activation provides the energy needed to overcome the barriers involved in plastic events. Irradiation, on the other hand, lowers certain barriers through random inelastic interactions. The activation of STZs leads to stress and strain redistribution which further assists the thermal activation of new STZs [44]. As

some simulations have shown, this coupling is likely to induce organization leading to the formation of shear bands [45]. This coupling may play a lesser role if the nucleation of plastic events is primarily determined by random interactions with the electron beam leading to plastic delocalization. We can speculate that this is one possibility to explain the very high stability of plastic deformation we observe up to very high strains. Further advanced TEM are required to unravel possible links between these mechanisms and local fluctuation of the atomic density, the chemical composition or the local atomic order [46].

5. Conclusion

We show that a-olivine thin films exhibit a significant ductility at room temperature. Under tensile loading with the electron beam off, a maximum stress of about 2.5 GPa is attained and a strain of 29 % can be reached. The stress-strain curve shows a stress maximum resulting from the response of the device to the increasing strain-rate with strain. The key finding of this study is the sensitivity of a-olivine to electron irradiation, which leads to a significant increase in ductility. An in-depth EELS study of the response of a-olivine under electron irradiation as a function of dose, but above all of acceleration voltage, led to the following conclusions. At low voltages (80 kV in our case), the predominant damage mechanism is radiolysis, clearly demonstrated by the release of molecular oxygen. At high voltages (300 kV), damage is mainly the result of knock-on that ablates the sample. The 200 kV voltage corresponds to the least damaging conditions for a-olivine since radiolysis is less than at 80 kV and knock-on is less than at 300 kV. The fact that irradiation enhanced ductility already observed at 200 kV is even more pronounced at 80 kV leads us to conclude that the mechanism responsible for this effect is radiolysis which promotes the breaking of Mg-O bonds.

Data availability

On reasonable request to the authors

CRediT authorship contribution statement

Andrey Orekhov: Writing – review & editing, Writing – original draft, Validation, Methodology, Investigation, Formal analysis. **Nicolas Gauquelin:** Writing – review & editing, Writing – original draft, Validation, Investigation, Formal analysis. **Guillaume Kermouche:** Writing – review & editing, Writing – original draft, Validation, Formal analysis. **Alejandro Gomez-Perez:** Writing – review & editing, Writing – original draft, Validation, Formal analysis. **Paul Baral:** Writing – review & editing. **Ralf Dohmen:** Writing – review & editing, Writing – original draft, Resources. **Michaël Coulombier:** Writing – review & editing, Resources. **Johan Verbeeck:** Writing – review & editing, Resources. **Jean Pierre Raskin:** Writing – review & editing, Resources. **Thomas Pardoen:** Writing – review & editing, Validation. **Dominique Schryvers:** Writing – review & editing, Validation, Resources. **Jun Lin:** Writing – original draft, Formal analysis. **Patrick Cordier:** Writing – review & editing, Writing – original draft, Validation, Funding acquisition, Conceptualization. **Hosni Idrissi:** Writing – review & editing, Writing – original draft, Validation, Methodology, Conceptualization.

Declaration of competing interest

The authors declare that they have no known competing financial interests or personal relationships that could have appeared to influence the work reported in this paper.

Acknowledgements

innovation programme under grant agreement No 787198 – TimeMan. H. Idrissi is mandated by the Belgian National Fund for Scientific Research (FSR- FNRS). This work was supported by the FNRS under Grant PDR –T011322F and the Programme 'Actions de Recherche concertées (ARC)' of the Fédération Wallonie-Bruxelles (re: project 'NanoGG' ref. nbr. 23/27–132).

Supplementary materials

Supplementary material associated with this article can be found, in the online version, at doi:10.1016/j.actamat.2024.120479.

References

[1] P. Richet, F. Leclerc, L. Benoist, Melting of forsterite and spinel, with implications for the glass transition of Mg$_2$SiO$_4$ liquid, J. Geophys. Res. 20 (1993) 1675–1678, https://doi.org/10.1029/93GL01836.

[2] R. Jeanloz, T.J. Ahrens, J.S. Lally, G.L. Nord, J.M. Christie, A.H. Heuer, Shock-produced olivine glass: first observation, Science 197 (1977) 457–459, https://doi.org/10.1126/science.197.4302.457.

[3] A. Lacam, M. Madon, J.P. Poirier, Olivine glass and spinet formed in a laser heated, diamond-anvil high pressure cell, Nature 288 (1977) 155–157, https://doi.org/10.1038/288155a0.

[4] J. Gasc, S. Demouchy, F. Barou, S. Koizumi, P. Cordier, Creep mechanisms in the lithospheric mantle Inferred from deformation of iron-free forsterite aggregates at 900-1200°C, Tectonophysics 761 (2019) 16–30, https://doi.org/10.1016/j.tecto.2019.04.009.

[5] H. Idrissi, P. Carrez, P. Cordier, On amorphization as a deformation mechanism under high stresses, Curr. Opin. Solid State. Mater. Sci. 26 (1) (2022) 100976, https://doi.org/10.1016/j.cossms.2021.100976.

[6] V. Samae, P. Cordier, S. Demouchy, C. Bollinger, J. Gasc, S. Koizumi, A. Mussi, D. Schryvers, H. Idrissi, Stress-induced amorphization triggers deformation in the lithospheric mantle, Nature 591 (2021) 82–86, https://doi.org/10.1038/s41586-021-03238-3.

[7] G. Kermouche, G. Guillonneau, J. Michler, J. Teisseire, E. Barthel, Perfectly plastic flow in silica glass, Acta Mat 114 (2016) 146–153, https://doi.org/10.1016/j.actamat.2016.05.027.

[8] E.J. Frankberg, J. Kalikka, F.G. Ferré, L. Joly-Pottuz, T. Salminen, J. Hintikka, M. Hokka, S. Koneti, T. Douillard, B. Le Saint, P. Kreiml, M.J. Cordill, T. Epicier, D. Stauffer, M. Vanazzi, L. Roiban, J. Akola, F. Di Fonzo, E. Levänen, K. Masenelli-Varlot, Highly ductile amorphous oxide at room temperature and high strain rate, Science 366 (2019) 864–869, https://doi.org/10.1126/science.aav1254.

[9] K. Zheng, C. Wang, Y.Q. Cheng, Y. Yue, X. Han, Z. Zhang, Z. Shan, S.X. Mao, M. Ye, Y. Yin, E. Ma, Electron-beam-assisted superplastic shaping of nanoscale amorphous silica, Nature Comm. 1 (2010) 24, https://doi.org/10.1038/ncomms1021.

[10] R. Dohmen, H.-W. Becker, E. Meißner, T. Etzel, S. Chakraborty, Production of silicate thin films using pulsed laser deposition (PLD) and applications to studies in mineral kinetics, Eur. J. Mineral. 14 (2002) 1155–1168, https://doi.org/10.1127/0935-1221/2002/0014-1155.

[11] T. Egami, S.J.L. Billinge, Underneath the Bragg Peaks: Structural Analysis of Complex Materials, Pergamon Press, Oxford, UK, 2003. Elsevier: Amsterdam, The Netherlands.

[12] P. Juhas, T. Davis, C.L. Farrow, S.J.L. Billinge, PDFgetX3: a rapid and highly automatable program for processing powder diffraction data into total scattering pair distribution functions, J. Appl. Cryst. 46 (2013) 560–566, https://doi.org/10.1107/S0021889813005190.

[13] E-Pdfsuite–Software For Analysis of Amorphous and Nano Crystalline Materials, NanoMEGAS SPRL, Belgium, 2009.

[14] M. Abeykoon, C.D. Malliakas, P. Juhás, E.S. Božin, M.G. Kanatzidis, S.J.L. Billinge, Quantitative nanostructure characterization using atomic pair distribution functions obtained from laboratory electron microscopes, Z. für Krist. 227 (2012) 248–256, https://doi.org/10.1524/zkri.2012.1510.

[15] Y. Rakita, J.M. Hart, P.P. Das, S. Shahrezaei, D.L. Foley, S.N. Mathaudhu, S. Nicolopoulos, M.L. Taheri, S.J.L. Billinge, Mapping structural heterogeneity at the nanoscale with scanning nano-structure electron microscopy (SNEM), Acta Mat. 242 (2023) 118426, https://doi.org/10.1016/j.actamat.2022.118426.

[16] M. Coulombier, P. Baral, A. Orekhov, R. Dohmen, J.-P. Raskin, T. Pardoen, P. Cordier, H. Idrissi, On-chip very low strain rate rheology of amorphous olivine films, Acta Mat. 266 (2024) 119693, https://doi.org/10.1016/j.actamat.2024.119693.

[17] M. Ghidelli, A. Orekhov, A.Li Bassi, G. Terraneo, P. Djemia, G. Abadias, M. Nord, A. Béché, N. Gauquelin, J. Verbeeck, J.P. Raskin, D. Schryvers, T. Pardoen, H. Idrissi, Novel class of nanostructured metallic glass films with superior and tunable mechanical properties, Acta Mat. 213 (2021) 116955, https://doi.org/10.1016/j.actamat.2021.116955.

[18] V. Samae, R. Gatti, B. Devincre, T. Pardoen, D. Schryvers, H. Idrissi, Dislocation driven nanosample plasticity new insights from quantitative in situ TEM tensile testing, Sci. Rep. 8 (2018) 12012, https://doi.org/10.1038/s41598-018-30639-8.

[19] B. Mantisi, N. Sator, B. Sator, Structure and transport at grain boundaries in polycrystalline olivine: an atomic-scale perspective, Geochim. Cosmochim. Acta 219 (2017) 160–176, https://doi.org/10.1016/j.gca.2017.09.026.

[20] N. Jiang, Electron beam damage in oxides: a review, Rep. Prog. Phys. 79 (2016) 016501, https://doi.org/10.1088/0034-4885/79/1/016501.

[21] R.F. Egerton, Radiation damage to organic and inorganic specimens in the TEM, Micron 119 (2019) 72–87, https://doi.org/10.1016/j.micron.2019.01.005.

[22] S.K. Lee, J.F. Stebbins, The degree of aluminum avoidance in aluminosilicate glasses, Am. Min. 84 (1999) 937–945, https://doi.org/10.2138/am-1999-5-631.

[23] L.A.J. Garvie, Can electron energy-loss spectroscopy (EELS) be used to quantify hydrogen in minerals from the O K edge? Am. Min. 95 (2010) 92–97, https://doi.org/10.2138/am.2010.3290.

[24] B. Winkler, M. Avalos-Borja, V. Milman, A. Perlov, C.J. Pickard, J.R. Yates, Oxygen K-edge electron energy loss spectra of hydrous and anhydrous compounds, J. Phys. Condens. Matter 25 (2013) 485401, https://doi.org/10.1088/0953-8984/25/48/485401.

[25] H.O. Ayoola, C.-H. Li, S.D. House, C.S. Bonifacio, K. Kisslinger, J. Jinschek, W.A. Saidi, J.C. Yang, Origin and suppression of beam damage-induced Oxygen-K edge artifact from γ-Al$_2$O$_3$ using Cryo-EELS, Ultramicroscopy (2020) 113127, https://doi.org/10.1016/j.ultramic.2020.113127.

[26] H. Tait, Five Thousand Years of Glass, British Museum press, London, 1991.

[27] Y. Yue, K. Zheng, Strong strain rate effect on the plasticity of amorphous silica nanowires, Appl. Phys. Lett. 104 (2014) 231906, https://doi.org/10.1063/1.4882420.

[28] J. Luo, J. Wang, E. Bitzek, J.Y. Huang, H. Zheng, L. Tong, Q. Yang, J. Li, S.X. Mao, Size-dependent brittle-to-ductile transition in silica glass nanofibers, NanoLetters 16 (2016) 105–113, https://doi.org/10.1021/acs.nanolett.5b03070.

[29] J.A. Tangeman, B.L. Phillips, A. Navrotski, J.K.R. Weber, A.D. Wilson, T.S. Key, Vitreous forsterite (Mg$_2$SiO$_4$): synthesis, structure and thermochemistry, Geophys. Res. Lett. 28 (2001) 2517–2520, https://doi.org/10.1029/2000GL012222.

[30] P. Baral, A. Orekhov, R. Dohmen, M. Coulombier, J.-P. Raskin, P. Cordier, H. Idrissi, T. Pardoen, Rheology of amorphous olivine thin films characterized by nanoindentation, Acta Mat. 219 (2021) 117257, https://doi.org/10.1016/j.actamat.2021.117257.

[31] A.J. Storm, J.H. Stern, X.S. Ling, H.W. Zandbergen, C. Dekker, Electron-beam induced deformations of SiO$_2$ nanostructures, J. Appl. Phys. 98 (2005) 014307, https://doi.org/10.1063/1.1947391.

[32] M. Mačković, F. Niekiel, L. Wondraczek, E. Spiecker, Direct observation of electron-beam-induced densification and hardening of silica nanoballs by in situ transmission electron microscopy and finite element method simulations, Acta Mat. 79 (2014) 363–373, https://doi.org/10.1016/j.actamat.2014.05.046.

[33] S.G. Kang, K. Jeong, J. Paeng, W. Jeong, S. Han, J.P. Ahn, S. Boles, H.N. Han, I.S. Choi, Athermal glass work at the nanoscale: engineered electron-beam-induced viscoplasticity for mechanical shaping of brittle amorphous silica, Acta Mat. 238 (2022) 118203, https://doi.org/10.1016/j.actamat.2022.118203.

[34] S. Stangebye, Y. Zhang, S. Gupta, T. Zhu, O. Pierron, J. Kacher, Understanding and quantifying electron beam effects during in situ TEM nanomechanical tensile testing on metal thin films, Acta Mat. 222 (2022) 117441, https://doi.org/10.1016/j.actamat.2021.117441.

[35] L.W. Hobbs, Electron-beam sensitivity in inorganic specimens, Ultramicroscopy 23 (1987) 339–344, https://doi.org/10.1016/0304-3991(87)90244-0.

[36] D.L. Griscom, Nature of defects and defect generation in optical glasses, Proc. Soc. Photo Opt. Instrum. Eng. 541 (1985) 38–59, https://doi.org/10.1117/12.975358.

[37] K. Kajihara, M. Hirano, L. Skuja, H. Hosono, Intrinsic defect formation in amorphous SiO$_2$ by electronic excitation: bond dissociation versus Frenkel mechanisms, Phys. Rev. B 78 (2008) 094201, https://doi.org/10.1103/PhysRevB.78.094201.

[38] L.W. Hobbs, Radiation effects in analysis of inorganic specimens by TEM, in: J.J. Hren, J.I. Goldstein, D.C. Joy (Eds.), Introduction to Analytical Electron Microscopy, Springer US, Boston, MA, 1979, pp. 437–480.

[39] C.F. Blanford, C.B. Carter, Electron radiation damage of MCM-41 and related materials, Microsc. Microanal. 9 (3) (2003) 245–263, https://doi.org/10.1017/S1431927603030447.

[40] J. Lin, C. Grygiel, A. Alessi, S. Dourdain, J. Causse, N. Ollier, O. Cavani, C. Rey, G. Toquer, X. Deschanels, A multiparametric study on the behavior of mesoporous silica under electron irradiation, Materialia 32 (2023) 101903, https://doi.org/10.1016/j.mtla.2023.101903.

[41] J.B. Pedley, E.M. Marshall, Thermochemical Data for Gaseous Monoxides, J. Phys. Chem. Ref. Data 12 (1983) 967–1031, https://doi.org/10.1063/1.555698.

[42] A.S. Argon, Plastic deformation in metallic glasses, Acta Metall 27 (1979) 47, https://doi.org/10.1016/0001-6160(79)90055-5.

[43] M.L. Falk, J.S. Langer, Dynamics of viscoplastic deformation in amorphous solids, Phys. Rev. E 57 (1998) 7192, https://doi.org/10.1103/PhysRevE.57.7192.

[44] T. Albaret, A. Tanguy, F. Boioli, D. Rodney, Mapping between atomistic simulations and Eshelby inclusions in the shear deformation of an amorphous silicon model, Phys. Rev. E 93 (2016) 053002, https://doi.org/10.1103/PhysRevE.93.053002.

[45] E.R. Homer, Examining the initial stages of shear localization in amorphous metals, Acta Mat. 63 (2014) 44–53, https://doi.org/10.1016/j.actamat.2013.09.050.

[46] H. Idrissi, M. Ghidelli, A. Béché, S. Turner, S. Gravier, J.J. Blandain, J.P. Raskin, D. Schryvers, T. Pardoen, Atomic-scale viscoplasticity mechanisms revealed in high ductility metallic glass films, Sci. Rep. 9 (2019) 13426, https://doi.org/10.1038/s41598-019-49910-7.